Targeted photodynamic therapy: Gluconamide-modified cellulose nanocrystals as efficient photosensitizer delivery platforms against Gram-negative bacteria

Ruth Prieto-Montero [a,b,**], Maite Tejón [a], Andrea Albaya [c], Teresa Arbeloa [a], Jose Luis Chiara [c], Mónica L. Fanarraga [b,**], Virginia Martínez-Martínez [a,*]

[a] *Departamento de Química Física, Universidad del País Vasco-EHU, Facultad de Ciencia y Tecnología, Apartado 644, 48080 Bilbao, Spain*
[b] *Grupo de Nanomedicina-IDIVAL, Universidad de Cantabria, Herrera Oria s/n, CP 39011 Santander, Spain*
[c] *Instituto de Química Orgánica General (IQOG-CSIC), Juan de la Cierva 3, 28006 Madrid, Spain*

ARTICLE INFO

ABSTRACT

Antimicrobial Photodynamic Therapy (aPDT) is an emerging strategy against resistant pathogenic bacteria, a serious global health threat. We describe herein the efficient preparation of photosensitized cellulose nano-crystals (CNC) using trialkoxysilane linkers for covalent incorporation of anionic (Rose Bengal: RB) and cationic (Toluidine blue O: TBO) photosensitizers (PSs), along with a *N*-alkyl-D-gluconamide ligand to specifically target *Escherichia coli*, as model nanosystems for aPDT. The synthesized nanomaterials exhibited high PS loading, high singlet oxygen quantum yield comparable to the solution, and good stability in aqueous media with minimal PS release under physiological conditions. Experimental viability tests in bacteria demonstrated their capability for aPDT, mitigating the inherent cytotoxicity of both PSs under dark conditions while retaining high phototoxicity against *E. coli* bacteria. The presence of gluconamide further enhanced photoactivity, highlighting the impor-tance of surface functionalization with a specific bacterial ligand for improved efficacy. The CNC-supported RB system exhibited sufficient fluorescence for tracking via fluorescence microscopy, making it suitable for thera-nostics, integrating bioimaging and aPDT. Overall, photosensitized CNCs hold great promise as nanocarriers for combating topical infections caused by Gram-negative bacteria, addressing the urgent need for novel therapeutic strategies in infectious disease management while also mitigating antimicrobial resistance.

1. Introduction

Antimicrobial resistance (AMR) has emerged as a significant challenge to public health, leading to approximately 700,000 casualties annually (Nikaido, 2009; Ran et al., 2021; Songca & Adjei, 2022; Will-yard, 2017; Wright, 2015). The incorrect and excessive use of antibiotics has resulted in a majority of microbials becoming resistant to the drugs used to treat them (Laxminarayan et al., 2016). As a consequence, pa-tients often face prolonged hospital stays, leading to increased treatment costs and, in the worst-case scenario, mortality (Luepke et al., 2017). In Europe, AMR causes at least 1500 million euros of losses and healthcare expenses (Antoñanzas & Goossens, 2019; Cassini et al., 2019). For that reason, new strategies and drugs are urgently required to combat AMR.

However, the development of new antibiotics presents several significant obstacles including limited financial incentives due to a small market compared to other therapeutic areas, stringent regulatory requirements that prolong the approval process and increase development costs, short treatment courses that limit profitability compared to drugs for chronic conditions, and discovery challenges in finding effective compounds with unique mechanisms of action against resistant bacteria without causing harm to the host organism. Moreover, the lengthy approval processes for new antibiotics facilitate that bacteria develop resistance even before the new drugs receive regulatory approval (Banin, Hughes, & Kuipers, 2017; Jørgensen et al., 2016; Ran et al., 2021; Tacconelli et al., 2018).

Currently, antimicrobial photodynamic therapy (aPDT), based on

the application of suitable light to a photoactive compound, (Hu, Huang, Wang, Wang, & Hamblin, 2018; Ran et al., 2021; Songca & Adjei, 2022; Yin & Hamblin, 2015) commonly known as a photosensitizer (PS), able to generate reactive oxygen species (ROS) from environmental molecular oxygen, is considered a complementary treatment. In general, ROS, and particularly singlet oxygen $^1O_2$ (photophysical mechanism depicted in Fig. 1), exhibit high reactivity, potentially leading to damage to biomolecules such as proteins, lipids, and nucleic acids. As a result, they can be cytotoxic to neighboring cells, bacteria, and fungi (Broekgaarden, Weijer, van Gulik, Hamblin, & Heger, 2015; DeRosa, 2002; Hu et al., 2018; Nonell & Flors, 2016; Sarbadhikary, George, & Abrahamse, 2021; Triesscheijn, Baas, Schellens, & Stewart, 2006). The local action, activated within the irradiated area and coupled with the short lifetime of $^1O_2$, hampers the development of resistance mechanisms in microorganisms. Note that this is also the reason why PDT is only effective in areas proximal to PSs, highlighting the crucial importance of precisely locating PSs to ensure effective treatment. In addition to selectivity, PSs need to fulfill the following criteria to be implemented in aPDT: i) minimal or no toxicity under dark conditions; ii) limited in vivo stability after irradiation to minimize secondary effects (such as skin photosensitization); iii) high singlet oxygen production yield; and iv) intense absorption ($\varepsilon \geq 50,000$ M^{-1} cm^{-1}) preferentially in the phototherapeutic window (Lacombe & Pigot, 2016) (630–850 nm), and v) significant solubility in aqueous media (DeRosa, 2002).

While PSs typically exhibit hydrophobic characteristics, leading to poor solubility in water and limited specificity for cellular uptake, the incorporation of specific water-soluble bioactive compounds alongside nanoparticles is anticipated to improve their pharmacokinetics. A variety of nanomaterials have been employed in photodynamic therapy (PDT) for enhanced drug biodistribution and uptake, targeting both bacteria and cancer cells (Awad, Thomas, Barnes, & Prestidge, 2022; Dai, Du, & Han, 2019; Kaya et al., 2020; Koshani, Zhang, Van De Ven, Lu, & Wang, 2021; Lucky, Soo, & Zhang, 2015; Mirzahosseinipour, Khorsandi, Hosseinzadeh, Ghazaeian, & Shahidi, 2020; Planas et al., 2015; Prieto-Montero, Arbeloa, & Martínez-Martínez, 2023; Qiao et al., 2020; Wu et al., 2020; Yin & Hamblin, 2015). In this work, cellulose nanocrystals (CNC) have been selected as suitable PS-carriers (Alvarado, Argyropoulos, Scholle, Peddinti, & Ghiladi, 2019; Do, Grijalvo, Imae, Garcia-Celma, & Rodríguez-Abreu, 2021; Klemm, Heublein, Fink, & Bohn, 2005; Navarro & Bergström, 2014; Thanh & Green, 2010; Vilarinho, Sanches Silva, Vaz, & Farinha, 2017). Cellulose is the most abundant organic biopolymer on Earth being biodegradable,

hydrophilic, and biocompatible (Das, Ghosh, & Sarkar, 2022; Do et al., 2021; Hemraz et al., 2015; Klemm et al., 2005; Malekpour, Hazrati, Khosrojerdi, Roshangar, & Ahmadi, 2023; Pinto et al., 2021; Thanh & Green, 2010; Vilarinho et al., 2017). Its carbohydrate structure is based on the repeated 1,4-connection of β-D-glucose building blocks (Do et al., 2021; Klemm et al., 2005; Vilarinho et al., 2017) (see Fig. 2a), presenting a high amount of hydroxy groups in their external surface area (Do et al., 2021), although not all of them are highly accessible and therefore reactive (Chauhan & Yan, 2015). These organic groups could be easily functionalized with molecules of interest such as PS and specific ligands (Alvarado et al., 2019; Klemm et al., 2005; Thanh & Green, 2010; Vilarinho et al., 2017). A variety of ligands, including proteins, polysaccharides, nucleic acids, peptides, and small molecules, can be attached to the surface of cellulose to improve the targeting of the PSs (Klausen, Ucuncu, & Bradley, 2020; Planas et al., 2015; Prieto-Montero et al., 2023; Zhao et al., 2017). In this context, photosensitized cellulose-based hybridized carriers are documented in the literature as interesting nanoplatforms for biomedical applications and, in particular, PDT (Decraene, Pratten, & Wilson, 2006; Feese, Sadeghifar, Gracz, Argyropoulos, & Ghiladi, 2011; Koshani et al., 2021; Monteiro, Neves, Nativi, Almeida, & Faustino, 2023).

Although high toxicity can be induced by photogenerated singlet oxygen in both Gram-positive and Gram-negative bacteria, it is important to note that the effectiveness of aPDT in Gram-negative bacteria is generally lower compared to Gram-positive bacteria. This difference is attributed to the presence of the additional outer layer in the cell membrane of Gram-negative bacteria, composed of negatively charged lipopolysaccharides, phospholipids and proteins (Kömerik, Wilson, & Poole, 2000). This layer poses challenges for the penetration of many compounds particularly those with a negative charge (Blázquez-Moraleja, Moya, Marin, & Bosca, 2023; Kaya et al., 2020; Lacey & Phillips, 2001; Mas et al., 2013; Q. Mesquita, J. Dias, P. M. S. Neves, Almeida, & F. Faustino, 2018), but also to the permeability depth of singlet oxygen as has been previously demonstrated (Dahl, Midden, & Hartman, 1989; Pucelik & Dąbrowski, 2022; Sułek et al., 2019). For these reasons, it is important to propose new photosensitized systems to improve aPDT in Gram-negative bacteria able to quickly and efficiently destroy these microorganisms when exposed to light. Cardoso (Capeletti et al., 2019) has recently reported on the use of open-chain carbohydrate derivatives, such as N-alkyl-D-gluconamides, to specifically target Gram-negative (GN) bacteria cells with silica nanoparticles (Fig. 2b). They have theoretically and empirically demonstrated the high binding affinity of gluconamides to the lipopolysaccharide region of the bacterial membrane, enabling the specific targeting of the pathogen cell wall. In addition, they found that gluconamide functionalization effectively prevented protein biofouling on the nanosystem, exhibiting no cytotoxicity and enhancing biocompatibility by mitigating the hemolytic effects observed in non-functionalized silica nanoparticles (Capeletti et al., 2019). Consequently, we anticipated that the presence of gluconamide on the CNC surface would enhance the suspension stability in various biological media, thereby prolonging their efficacy and lifespan within the body.

In this work, we describe the preparation, photophysical properties, and antimicrobial activity of photosensitized CNC functionalized with standard anionic (Rose Bengal: RB) and cationic (Toluidine Blue O: TBO) photosensitizers, together with a N-alkyl-D-gluconamine targeting substituent in order to enhance CNC selectivity for Gram-negative bacteria, particularly *Escherichia coli* (*E. coli*) (Fig. 2b–c). RB is a widely known and commercially available PS with an absorption band centered in the green region ($\lambda_{abs} \approx 560$ nm) of the visible spectrum, along with high singlet oxygen production ($\phi_\Delta = 0.50$–0.90) (DeRosa, 2002; Lacombe & Pigot, 2016; Martínez, Braun, & Oliveros, 2004), modest fluorescence ($\phi_{fl} = 0.10$) (Prieto-Montero et al., 2021), and high phototoxicity against Gram-positive bacteria. However, RB is considered a priori unsuitable for Gram-negative bacteria due to its inherent negative charge (George, Hamblin, & Kishen, 2009). Regarding TBO, it is one of the most
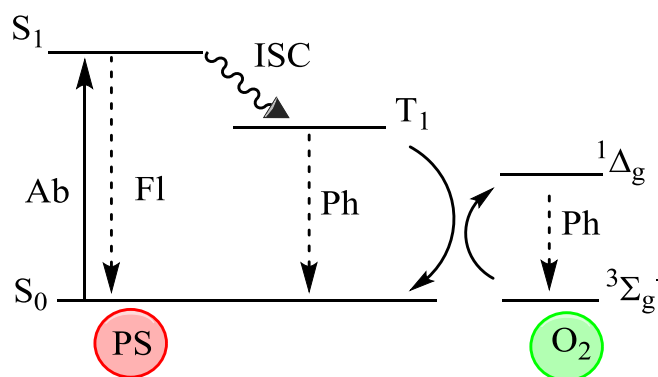
Fig. 1. Schematic description of singlet oxygen generation by the photosensitizer (PS): the PS adsorbs radiation and transitions to its excited singlet state ($S_0 \rightarrow S_1$). After an intersystem crossing process (ICS), its triplet excited state is populated. The triplet state of PS transfers its energy to environmental oxygen generating singlet oxygen. S_0 = ground state, S_1 = first excited singlet state, Ab = absorption, Fl = fluorescence, ISC = intersystem crossing, Ph = phosphorescence, T_1 = first excited triplet state, $^3\Sigma_g^-$ = fundamental state of molecular oxygen, which corresponds to its triplet state and $^1\Delta_g$ = first excited state of molecular oxygen, commonly denoted singlet oxygen ($^1O_2$).
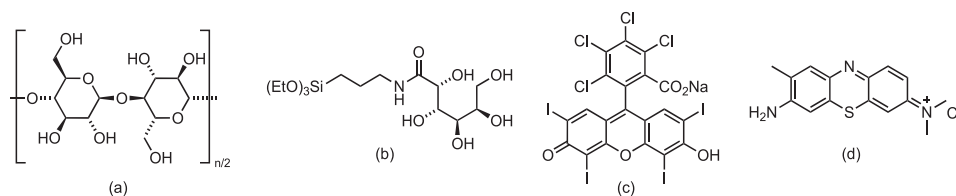
Fig. 2. (a) Cellulose, (b) *N*-(3-triethoxysilylpropyl) gluconamide, (c) Rose Bengal, (d) Toluidine Blue O.

commonly used PSs in aPDT against both Gram-positive and Gram-negative bacteria, particularly in treating dental and accessible skin infections (Carrera et al., 2016). Its absorption band is located in the red region ($\lambda_{abs} \approx 630$ nm) (Lacombe & Pigot, 2016) and exhibits also high singlet oxygen generation ($\phi_\Delta = 0.50$–0.80) (Chen, Cesario, & Rentzepis, 2010; Mariño-Ocampo, Reyes, Günther, Heyne, & Fuentealba, 2022), but poor fluorescence quantum yield ($\phi_{fl} < 0.10$).

2. Experimental

2.1. Materials

Starting spray-dried CNC used in this work was acquired from CelluForce, Inc. (Montreal, QC, Canada). The received material had the following product specifications (measured by the National Research Council of Canada): particle diameter (crystallite): 2.3–4.5 nm (by AFM); particle length (crystallite): 44–108 nm (by AFM); crystalline fraction: 0.88 (by XRD); sulfur content: 0.86–0.89 %; sulfate content: 246–261 mmol/kg. Rose Bengal (RB, Sigma-Aldrich), ethyl chloroformate (Across), triethylamine (Sigma-Aldrich), (3-aminopropyl)trimethoxysilane (APTMS, Sigma-Aldrich), *N*-(3-triethoxysilylpropyl)-D-gluconamide ("gluconamide", Gelest), Toluidine O (TBO, Sigma-Aldrich), (3-glycidyloxypropyl)trimethoxysilane (GOPS, Sigma-Aldrich) were obtained from the indicated commercial sources.

2.1.1. CNC functionalization with Rose Bengal and gluconamide

To a stirred solution of Rose Bengal (26.4 mg, 0.026 mmol) in anhydrous methanol (20 mL, Sigma-Aldrich) under a nitrogen atmosphere at 0 °C was added dropwise ethyl chloroformate (3 μL, 0.026 mmol) and triethylamine (4 μL, 0.026 mmol). After stirring the reaction mixture for 30 min, (3-aminopropyl)trimethoxysilane (5 μL) was added and the mixture was stirred for 1 h at 0 °C. CNC (30 mg) and *N*-(3-triethoxysilylpropyl)-D-gluconamide were added (11 μL, 0.026 mmol) and the mixture was stirred for 1 h at room temperature. The resultant suspension of fully functionalized CNC with RB and gluconamide (RB-Glu@CNC) was centrifuged (15,000 rpm, 21,130 rcf) and washed with ethanol until a colorless supernatant was obtained. The RB-Glu@CNC was collected by filtration (see Supporting Information, Scheme S1). As a control sample, CNC only with attached RB and without gluconamide (RB@CNC) and CNC only with tethered gluconamide without RB (Glu@CNC) were also synthesized following similar procedures.

2.1.2. CNC functionalization with Toluidine Blue O and gluconamide

To covalently link Toluidine Blue O (TBO) to the hydroxy groups of the CNC surface, two steps are required. First, to a stirred suspension of CNCs (30 mg) in anhydrous methanol (20 mL) under a nitrogen atmosphere at room temperature was added (3-glycidiloxypropyl)trimethoxysilane (6 μL, 0.026 mmol). After stirring for 3 h, CNCs were centrifuged (15,000 rpm, 21,130 rcf) and washed with ethanol and collected by filtration (see Supporting Information, Scheme S2a). In the second step, this CNC (30 mg) functionalized with epoxide groups was suspended in anhydrous methanol (20 mL) under a nitrogen atmosphere at room temperature and TBO (7.94 mg, 0.026 mmol) and *N*-(3-triethoxysilylpropyl)-D-gluconamide (11 μL, 0.026 mmol) were added to the flask, and the mixture was stirred at room temperature for 3 h. Finally, the resultant suspension of functionalized CNC with TBO and

gluconamide (TBO-Glu@CNC) was centrifuged (15,000 rpm, 21,130 rcf) and washed with ethanol until a colorless supernatant was obtained. The TBO-Glu@CNC were collected by filtration (see Supporting Information, Scheme S2b).

Importantly, the amount of TBO physically attached by electrostatic forces to the CNC surface was removed by suspending the TBO-Glu@CNC sample in aqueous NaCl (1 M) solution and stirring for 2 h, followed by centrifugation (15,000 rpm, 21,130 rcf) and washing with water. This process was carried out three times before the final system, named as TBO-Glu@CNC-w, was collected by filtration.

2.2. Material characterization

The size, shape, and morphology of the obtained CNCs were characterized by transmission electron microscopy (TEM) using a JEOL JEM 1400Plus operating at 100 kV. Images were acquired with a sCMOS Hamamatsu digital camera, and the CNCs (0.33 mg/mL) were stained with 10 μL of uranyl acetate (0.5 % in H₂O). Dynamic light scattering (DLS) and Zeta potential (ZP) measurements to analyze the NP hydrodynamic diameter and suspension electrophoretic stability were carried out using a Malvern Zetasizer Nano ZS, which has a HeliUM-Neon ($\lambda = 633$ nm) laser. FTIR spectra were obtained from powder samples using the ATR technique with an Affinity-1S Shimadzu spectrometer (4000–400 cm^{-1} range). All CNC samples, both unmodified and modified, were characterized by solid-state cross-polarization/magic angle spinning (CP-MAS) ^{13}C NMR spectroscopy using a Bruker AV 400 WB spectrometer operating at a ^{13}C NMR frequency of 100.62 MHz. Spectra were acquired at a magic angle spinning rate of 7 kHz using 4 mm ZrO₂ rotors. Data processing and peak deconvolution were performed using MestReNova 15.0.1 software.

The absorption spectra were recorded with a UV–Vis-NIR spectrometer (model Cary 7000, Agilent Technologies). In the case of the nanoparticle samples, an integrating sphere (model Internal DRA 900, Livingston, UK) was used for uniform light collection to correct for reflection and scattering effects of the samples. The fluorescence measurements were recorded with an Edinburgh Instruments Spectrofluorimeter (FLSP920 model, Livingston, UK) equipped with a 450 W xenon flash lamp as the excitation source. The fluorescence spectra were corrected from the wavelength dependence on the detector sensibility. The fluorescence quantum yields of the photosensitizers were measured by the relative method, using different standard sample dyes depending on the spectral region: PM597 ($\Phi_{fl} = 0.48$ in methanol) (Prieto, Arbeloa, Martínez, López, & Arbeloa, 2004) for RB and cresyl violet ($\Phi_{fl} = 0.54$ in methanol) (Magde, Brannon, Cremers, & Olmsted, 1979) for TBO. The singlet oxygen (^{1}O₂) production was determined by direct measurement of its phosphorescence at 1276 nm, Fig. S2, employing an NIR detector (InGaAs detector, Hamamatsu G8605-23), integrated into the same Edinburgh spectrofluorimeter upon continuous monochromatic excitation (450 W Xenon lamp) of the sample. Singlet oxygen quantum yields (Φ_Δ^{PS}) were calculated by the relative method, using commercial photosensitizers as references: Rose Bengal (RB, $\Phi_\Delta^{PS} = 0.86$ in CH₃OD) (Prieto-Montero et al., 2021), and New Methylene Blue (NMB, $\Phi_\Delta^{PS} = 0.76$ in CH₃OD) (Prieto-Montero et al., 2022), Eq. (1). Φ_Δ^R is the quantum yield of singlet oxygen production of the reference. The factor $\alpha = 1$–10^{-A}, corrects the different numbers of photons absorbed by the samples (being A the absorbance at the excitation wavelength), S_e is the

initial singlet oxygen signal of the samples at 1276 nm (Fig. S2).

$$\Phi_\Delta^{PS} = \Phi_\Delta^R \frac{S_e^{PS}}{S_e^R} \frac{\alpha^R}{\alpha^{PS}} \tag{1}$$

The amounts of PSs attached to CNC were estimated photometrically for PS@CNC stable suspensions, assuming the same molar extinction coefficients for the PSs in solution and those covalently attached at the CNC surface.

To study the PS release, dialysis assays were carried out with RB-Glu@CNC, TBO-Glu@CNC, and TBO-Glu@CNC-w in PBS at r.t. For this, a pre-stirred PS@CNC suspension (5 mg/mL in 1 mL PBS) was transferred to a dialysis tube (3.5–5 kD Float-ALyzer), and the tube was immersed in 60 mL of PBS kept under magnetic stirring at r.t (Fig. S11). Aliquots were taken at different times to assess the concentration of unbound PS by photometric method, measuring the absorbance of the aliquot and extrapolating their concentration by calibration curves following Beer's law.

2.3. Antibacterial activity

Recombinant *E. coli* bacterial strains, engineered to overexpress a green fluorescent protein (GFP) mutant protein in the presence of iso-propyl β-D-1-thiogalactopyranoside (IPTG) described elsewhere (García-Hevia et al., 2021), were utilized to specifically identify viable bacteria by observing the production of GFP fluorescence. The protocol followed to expose the bacteria to the different PSs in solution or PS@CNCs is depicted in Scheme S3. Briefly, the bacterial precultures were regrown until they reached an optical density (OD) of 0.6. A total of 750 μL of these cultures were aliquoted and resuspended in PBS. For light exposure, 50 μL aliquots of this *E. coli* suspension were placed in the wells of a 24-well plate, followed by the addition of various solutions or dispersions of the PS and PS@CNC. To ensure an even distribution of the added compounds, the plate was vigorously shaken at 500 rpm for 30 min before irradiation. Irradiations were performed using light-emitting diode devices: LED Par 64 Short Q4-18 (Showtec, Burgebrach, Holland) for the green region (wavelength centered at 518 nm) and LED 36 W (KINGBO LED) for red (wavelength centered at 655 nm), as shown in Scheme S3. The irradiation time depends on the fluence rate of each LED according to Eq. (2):

$$TLD \ \left(J/cm^2\right) = fluencerate \ \left(mW/cm^2\right) \times treatment \ time \ (s) \tag{2}$$

The total light dosage (TLD) was optimized for green light irradiation by varying the exposition time: 30 min (16 J/cm^2), 60 min (32 J/cm^2), and 120 min (65 J/cm^2). In the case of the other experiments with red light, the optimal total light dosage of 65 J/cm^2 was used.

To assess bacterial viability post-treatment, *E. coli* bacterial suspensions were subjected to serial dilution, with 100 μL of each dilution plated onto LB agar plates (see Scheme S3 and Fig. S1). These plates were then incubated overnight at 37 °C, after which the number of viable bacteria was determined by counting the colony-forming units (CFU). This count was compared to the untreated control group. Each condition was replicated three times, and each experiment was conducted on three separate days. Bacterial survival is expressed as the percentage relative to the control CFU count (under dark conditions). Statistical differences between the control and treated *E. coli* were assessed using a *t*-test through the GraphPad Prism program. The significance level grade is: *P* value: *<0.033, **<0.002, ***<0.0002, and ****<0.0001, $n = 3$, DF = 4.

2.4. Bacteria imaging

Confocal microscopy imaging was performed on bacteria mounted onto crystal glass coverslips. These were imaged using a Nikon A1R confocal microscope equipped with 5 lasers (405, 488, 514, 561, and 633 nm) and 4 filter-based detection channels. A 100×1.49 NA lens was

used for imaging. Image processing was performed with the NIS-Elements Advanced Research software. All images are pseudo-colored.

Imaging was performed on live GFP-expressing recombinant bacteria incubated in dark conditions with IPTG (0.5 μM) and with RB free or RB-Glu@CNC under 2 h. Afterward, the samples were mounted onto crystal glass coverslips. Hoechst, along with RB in solution or RB@CNC and RB-Glu@CNC nanoplatforms, was used to determine sample localization in *E. coli*.

Additionally, to visualize the phototherapy effect, GFP-expressing *E. coli* were incubated in an agar plate together with IPTG and RB-Glu@CNC. Only half of the bacterial culture plate was irradiated for 2 h, while the other half was kept in dark conditions.

For transmission electron microscopy (TEM) imaging the bacteria and nanoparticles, 150 μL of bacterial suspension, with OD = 0.6, were incubated with CNC and Glu@CNC (0.15 mg/mL) in PBS. After 2 h of incubation, the bacteria were fixed with 4 % paraformaldehyde for 20 min and washed with water four times. The samples were deposited on carbon-coated copper grids. Imaging was performed using a JEOL JEM 1011 operated at 100 kV equipped with a Gatan Orius Sc 1000 CCD camera (JEOL, Japan).

3. Results and discussion

3.1. Nanocelullose characterization

The starting CNC was characterized by TEM, DLS/Zeta potential, and ^{13}C CP-MAS NMR and FTIR-ATR to study its morphology, size distribution, stability in water, and chemical composition, respectively. According to TEM images (Fig. 3), the nanocellulose presented the typical rod-like shape, with a size distribution of around 110 ± 70 nm in length (Fig. S3), in good agreement with the hydrodynamic diameter value in H_2O (84 nm) obtained by DLS (Table S1) and the specifications of its commercial source (CelluForce, Inc.). The highly negative ζ-potential value (-32.0 mV) predicts a good stability in water, avoiding particle agglomeration and precipitation (Table S1) (Arulprakasajothi, Elango-van, Chandrasekhar, & Suresh, 2018; Bhattacharjee, 2016).

The FTIR-ATR spectrum (Fig. S4) showed its characteristic peaks at:
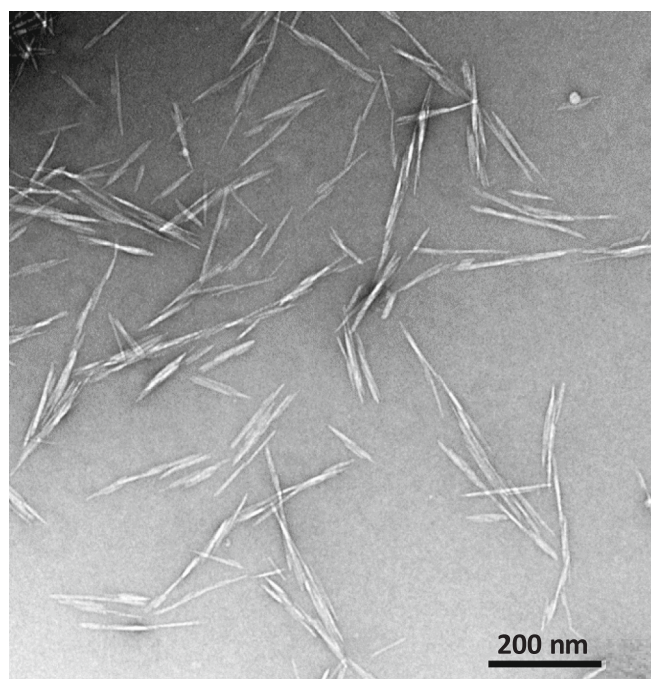
Fig. 3. TEM images of the starting cellulose nanocrystals (CelluForce) suspended in water and stained with 10 μL of uranyl acetate 0.5 % (Scale bar 200 nm).

3325 cm^{-1} assigned to the stretching of hydroxy groups, 2890 cm^{-1} associated with the stretching vibration of the C—H groups of the glucose unit and 1373 cm^{-1} to the bending vibration of H—C—C, 899 cm^{-1} attributed to the β-glycosidic bond between glucose units, at 1060 cm^{-1} corresponded to the C—O group from secondary alcohols and ethers of the cellulose vertebral column of the chain, at 1167 cm^{-1} characteristic of the symmetric stretching of the C—O—C group and the stretching band of C—C combined with absorbed water at 1640 cm^{-1} (Abderrahim et al., 2015; Sommer & Staroszczyk, 2023).

The ^{13}C CP-MAS NMR spectrum of neat CNCs from CelluForce (Fig. S6) showed characteristic signals consistent with cellulose I allomorph, featuring sharp resonances assigned to the C1-C6 carbons in the crystalline domains and broader peaks corresponding to the C4 and C6 carbons in the amorphous regions (Brinkmann et al., 2016). The C1 carbon resonances were observed at 104–106 ppm, C4 resonances at 84–89 ppm, C2/C3/C5 peaks in the 61–76 ppm region, and C6 peaks at 71–76 ppm.

3.2. Surface functionalization of CNC

The surface of CNC was functionalized with gluconamide (Glu), along with the two different photosensitizers RB and TBO of anionic and cationic nature, respectively, following the synthesis routes depicted in Schemes S1 and S2. The resultant samples are named Glu@CNC for CNC functionalized solely with gluconamide, and RB-Glu@CNC and TBO-Glu@CNC for CNC functionalized with RB and TBO together with Glu, respectively. RB@CNC corresponds to CNC with RB without Glu and TBO-Glu@CNC-w is the TBO-Glu@CNC sample after an exhaustive washing process.

The successful covalent attachment of the Glu biotargeting ligand was probed by FT-IR (Fig. S5a) by the presence of the new bands located at 1280 cm^{-1} and at 879 cm^{-1} assigned to the stretching vibration of CH$_2$-Si and Si—O groups, respectively and at 3335 cm^{-1} that corresponds to N—H stretching from the amide group of gluconamide. The characteristic stretching band of the C=O groups is likely peaked at 1645 cm^{-1} but cannot be undoubtedly assigned due to its overlapping with the OH bending of absorbed water (Ji et al., 2020). The covalent attachment of *N*-(3-triethoxysilylpropyl)-ᴅ-gluconamide (Glu) at the surface of CNC resulted in a small increase of the hydrodynamic diameter (from around 85 nm to 100 nm) and a minor change in the negative values of the ζ-potential (−32 to −35 mV) (Table S1), indicating a slightly better suspension stability of Glu@CNC compared to CNC without Glu.

The FTIR-ATR spectra of RB@CNC and TBO@CNC (Fig. S5b) showed new bands at 1602 cm^{-1} and 1545 cm^{-1}, (Al-Majmaie, Alattar, Zerulla, & Al-Rubeai, 2012; Rizzi et al., 2015), which correspond to the carbon-carbon stretching vibrations of the aromatic rings of RB and TBO. The corresponding ζ-potentials (Table S1) were very similar as in the case of Glu@CNC (−35.2 mV) despite the presence of the organophilic PSs, values below −25 mV ensuring a good stability of the aqueous suspensions.

In addition to the characteristic cellulose backbone signals (C1-C6), the ^{13}C CP-MAS NMR spectra of Glu@CNC, RB@CNC, RB-Glu@CNC, and TBO-Glu@CNC-w showed new low-intensity peaks attributable to the silane moiety (Figs. S7–S10). Specifically, resonances at 41–44 ppm, 22–23 ppm, and 10–11 ppm were assigned to the N—*CH$_2$*—*CH$_2$*—*CH$_2$*—Si carbon atoms, respectively, confirming the successful grafting of the silane coupling agent onto the CNC surface. Due to the low loadings observed and the non-quantitative nature of CP-MAS spectra, precise estimation of molar substitution ratios for the functionalized CNCs was not possible (see further discussion below). The weak ^{13}C NMR signals of the gluconamide substituent, expected to appear in the 64–73 ppm region (Chen, Zhang, Sui, Brennan, & Brook, 2005) were obscured by the prominent signals of the cellulose backbone.

The loading of PSs at the surface of the CNC samples was photometrically estimated (see Experimental section) (Table S1). For RB-Glu@CNC, PS content was 13.2 μmol/g, whereas a much higher dye loading of 58.4 μmol/g was measured for TBO-Glu@CNC. This difference was attributed to the positive charge of the TBO dye (Fig. 2), which can also be electrostatically attached to the partially negative CNC surface due to the presence of ionized hemisultate ester groups (Do et al., 2021). Thus, after extensive washing of TBO-Glu@CNC (see Experimental section) to remove non-covalently attached TBO molecules, we obtained the sample named TBO-Glu@CNC-w, wherein the final amount of chemically linked TBO was comparable to that of RB-Glu@CNC (Table S1).

The possible release of the PS from the surface of CNCs was analyzed by dialysis assays conducted at room temperature for 24 h for the three photosensitized nanosystems: RB-Glu@CNC, TBO-Glu@CNC, and TBO-Glu@CNC-w (Fig. S11, Table S2 and Fig. S12). For RB-Glu@CNC the percentage of PS released was <7 % after 24 h, indicating the robustness of the covalent link between RB and CNC. As expected, the behavior of the TBO-Glu@CNC system was very different, with near 50 % of the initial amount of TBO released under the same conditions (Fig. S12, Table S2). From the dialysis experiments, the quantity of TBO electrostatically adsorbed on the CNC surface was estimated to be 6 times higher than the TBO covalently anchored (Table S1). In comparison, the TBO-Glu@CNC-w sample, subjected to extensive washing to remove physically adsorbed TBO, showed a low level of TBO release (Table S2).

The photophysical properties (absorption, emission, and singlet oxygen production) of the PSs in solution and RB-Glu@CNC and TBO-Glu@CNC-w hybrid nanosystems (Fig. 4, Table 1) were studied in methanolic suspension. The absorption spectra of RB-Glu@CNC and TBO-Glu@CNC systems are similar (position and shape) to those recorded for the respective PS in methanol (Fig. 4), indicating the lack of dye aggregation. Regarding the singlet oxygen capacity, both PSs retain almost unaltered values (Table 1) when anchored to the surface of CNC, leading to a promising nanosystem to be implemented in aPDT.

In general, the fluorescence quantum yield values are low, as expected for PSs with relatively high singlet oxygen generation. However, RB is considered bright enough to be tracked by fluorescence microscopy (Prieto-Montero et al., 2021). (Prieto-Montero et al., 2021). Single *Z*-plane confocal microscopy images taken with a 100 × 1.49 NA lens show that the green fluorescence emission from live *E. coli* over-expressing GFP is correlative with the red fluorescence from RB (refer to the spectrogram profiles in Fig. 5) in two representative bacterial cells. To some extent, higher red emission brightness was detected for RB-Glu@CNC sample (Fig. S13).

In this context, RB is generally excluded from the interior of Gram-negative cells and remains at a superficial subcellular location. However, some published studies have noted that RB may slowly penetrate into bacteria with lengthier incubation time, allowing the accumulation of photosensitizer (with time) by a diffusion-driven process rather than affinity-mediated binding (Dahl, Midden, & Neckers, 1988; Demidova & Hamblin, 2005; Manoil, Filieri, Schrenzel, & Bouillaguet, 2016; Sabbahi, Ben Ayed, & Jemli, 2018). Conversely, when RB is covalently linked to CNC, the nanosystem is unlike to cross the membrane and will remain attached to the bacteria membrane.

3.3. Antimicrobial activity of the photosensitized CNCs

As an initial step, we assessed the inherent effect of the three hybrid nanosystems on *E. coli* cultures before light exposure. As a primary control, we confirmed that both, the irradiation source (green or red light) and the bare CNC nanoplatforms (at a concentration of 0.1 mg/mL) had a negligible cytotoxic effect on bacteria throughout the incubation period (Figs. S14 and S15).

Before testing the phototoxic effect of RB-Glu@CNC (and RB@CNC) and TBO-Glu@CNC systems under green and red irradiation, respectively, preliminary assays were conducted for RB and TBO dyes in solution (Figs. S16, S17 and S18). These assays initially assessed the cyto- and phototoxic effects at different concentrations, ranging from 5·10^{-7}
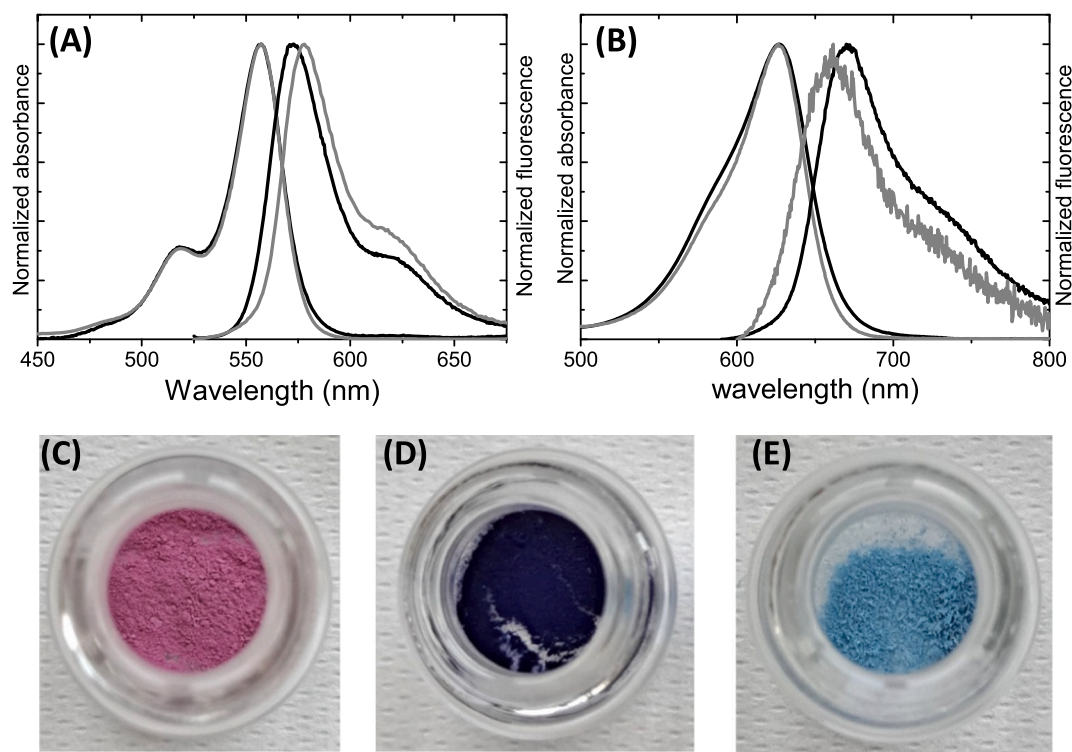
Fig. 4. Top) Normalized absorption and emission spectra of (A) RB-Glu@CNC (black) and RB in solution (grey) and (B) TBO-Glu@CNC-w (black) and TBO in solution (grey) and bottom) Powder images of (C) RB@CNC, (D) TBO-Glu@CNC (with TBO electrostatic and covalent linked), and (E) TBO-Glu@CNC-w (with TBO linked only covalently).

Table 1

Photophysical properties of PSs and PS-Glu@CNCs in methanol-d_4: absorption maxima (λ_{ab}), fluorescence maxima (λ_{fl}), fluorescent quantum yield (Φ_{fl}) and singlet oxygen quantum yield (Φ_Δ).

Name	Sample	λ_{ab} (nm)	λ_{fl} (nm)	Φ_{fl}	Φ_Δ
RB	Solution	556	578	0.10	0.86
RB-Glu@CNC	RB + Glu	555	576	0.09	0.74
TBO	Solution	628	662	0.02	0.56
TBO-Glu@CNC-w	TBO$_{covalent}$ + Glu	627	668	0.04	0.54

M to $1\cdot10^{-5}$ M, with incubation (and light irradiation) times fixed at 2 h. RB was observed to eradicate 100 % of the incubated bacteria over the concentration $5\cdot10^{-7}$ M (Fig. S16). Besides, RB exhibited a relatively high level of cytotoxicity under dark conditions, resulting in a 40–60 % reduction in bacterial viability. On the other hand, TBO in solution displayed significantly greater cytotoxicity leading to the complete eradication of bacteria in the absence of light (as shown in Fig. S17). To further study the cyto- and photo-toxicity effects and explore the synergetic effect of light in TBO, viability tests were run at lower incubation times (or light exposure times for the irradiated samples). The cytotoxicity was considerably reduced with 30 min and 10 min incubation times leading to 60 % and 70 % CFU bacteria viability, respectively, whereas no bacteria survival was found under light irradiation (Fig. S18), confirming the high phototoxicity action of the treatment on *E. coli*.

Variation in incubation times (and light doses) were also tested (Fig. S19) for RB-Glu@CNC system under green light (Fig. S19), to determine the optimal conditions for efficient phototoxic treatments. For that, viability experiments with different exposition times (30 min, 1 h and 2 h, which correspond to 16, 32 and 65 J/cm^2, respectively) were carried out. The results showed that the highest significant grades (***) with respect to dark control was achieved with 2 h of green

irradiation. Thus, all the following assessments were carried out at $5\cdot10^{-7}$ M and 65 J/cm^2, which were considered the best conditions for a comparative analysis of the samples.

In the case of RB, three different systems, free RB in solution, RB-Glu@CNC, and RB@CNC (without gluconamide as a ligand) were tested in *E. coli* in dark conditions and under green irradiation (Fig. 6). RB in solution displayed higher phototoxicity in comparison to RB-Glu@CNC and RB@CNC, leading to the lowest % CFU (12 %) with the highest grade of significance compared to the bacterial control (****), followed by RB-Glu@CNC (32 %, *** grade of significance) and RB@CNC (45 %, **). However, RB in solution also exhibited cytotoxic effects under dark conditions, resulting in approximately 60 % bacterial death (Fig. 6). This toxicity is mitigated when RB is immobilized on the surface of CNCs, showing a significant reduction (indicated by grades * and ** for RB@CNC and RB-Glu@CNC, respectively). Note that the causes of RB's cytotoxicity in solution under dark conditions remain unclear. However, previous studies have shown that cytotoxicity increases with longer incubation times or higher concentrations, possibly due to a membrane permeabilization process under these conditions (Atrash et al., 2024; Kurosu et al., 2022). Thus, one possible explanation for the suppression of the cytotoxicity effects for RB@CNC nanosystems is their inhibited ability to cross the bacteria membrane, providing a more secure approach to antimicrobial PDT by minimizing side effects associated with dark toxicity. Consequently, RB-sensitized CNC nanoplatforms show promise as a suitable carrier for implementing PDT.

The statistically significant differences in phototoxicity between free RB in solution and the RB@CNC sample under dark and light conditions confirm that the pronounced phototoxic effect of free RB in solution is partly due to its inherent toxicity, differing by a modest 31 % between dark and after light irradiation. In contrast, the differences between dark and light conditions found in both RB-Glu@CNC and RB@CNC systems are higher, ca. 50 %. Furthermore, the comparison of results between RB-Glu@CNC and RB@CNC reveals that the presence of gluconamide at the CNC surface enhances its photoactivity, demonstrating more
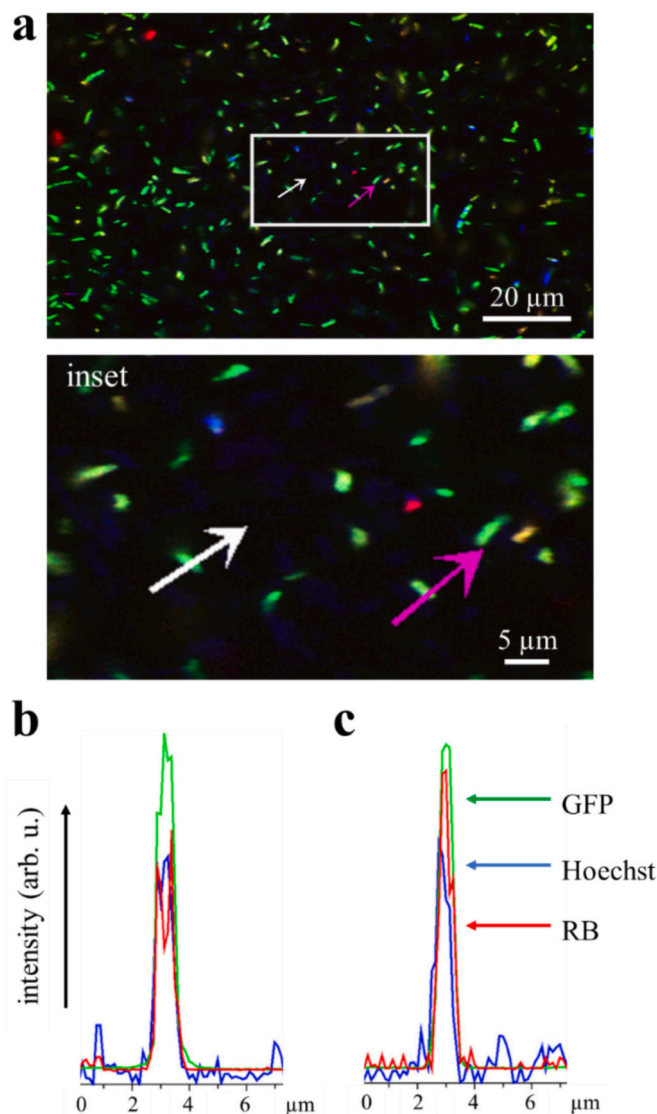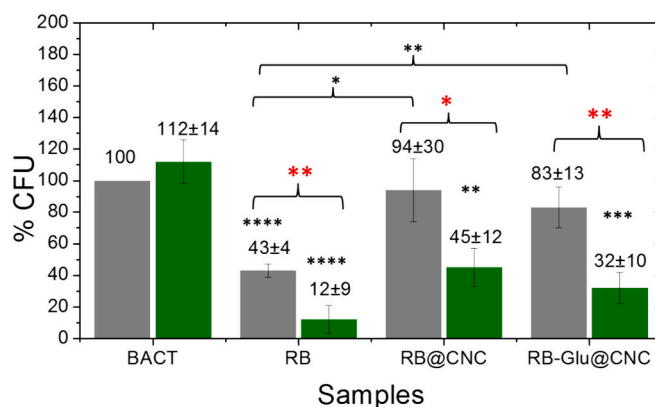
Fig. 5. (a) Confocal microscopy images of GFP-expressing *E. coli* cells (green channel) treated with RB-Glu@CNC (red channel) and stained with Hoechst (blue channel). Two arrows cross two live bacteria. (b–c) Corresponding spectrograms of the fluorescence at the cross-section of the white (b) and pink (c) arrows reveal distinct intensity profiles within the cells, confirming that these bacteria are alive and colocalize with RB.

Fig. 6. CFU % (as viability test) of *E. coli* bacteria under dark conditions (grey bar) and under 2 h of green irradiation (green bar) incubated with different systems: nothing (BACT), free RB in solution at the concentration of $5 \cdot 10^{-7}$ M (RB), RB@CNC (RB concentration of $5 \cdot 10^{-7}$ M without gluconamide) and the complete nanosystem RB-Glu@CNC (RB concentration of $5 \cdot 10^{-7}$ M with gluconamide). Black asterisks indicate a significant difference to controls. Red asterisks indicate significant differences between dark and light conditions at the same concentrations tested. P value: $* < 0.033$, $** < 0.002$, $*** < 0.0002$, and $**** < 0.0001$, $n = 3$, DF = 4.

significant differences for RB-Glu@CNC than RB@CNC when compared to the dark control (*** and **, respectively). This result underscores the importance of the presence of gluconamide molecules at the surface of CNC to improve the photoactivity, possibly due to a better interaction between RB-Glu@CNC and the bacterial cell wall. Taking into account that dried sample preparation for TEM may introduce artifacts, Fig. 7 shows representative TEM images of *E. coli* cells onto a carbon-coated grid. These images suggest a favorable interaction between Glu@CNC and the bacterial cell wall compared to CNC without gluconamide functionalization. When both samples are incubated at the same concentration, the interaction appears more pronounced with Glu@CNC (Fig. 7).

The efficacy of PDT is illustrated in the fluorescence image of RB-Glu@CNC-treated bacteria (Fig. 8), where only a portion of the *E. coli* colonies was exposed to green light, while the rest remained in darkness. After treatment, the covered (unexposed) culture section showed intense green emission indicative of live bacteria producing GFP, whereas virtually no live cells were observed in the irradiated area.

Regarding the second PS, three different systems were incubated with *E. coli* bacteria, free TBO in solution, TBO-Glu@CNC, and TBO-Glu@CNC-w (with TBO covalently and electrostatically, or only covalently attached, respectively). As stated, TBO in solution exhibited 100 % toxicity under dark conditions at a PS concentration of $5 \cdot 10^{-7}$ M (Fig. 9) and 2 h of incubation. Similar outcomes were observed for TBO-Glu@CNC, where TBO is physically absorbed by electrostatic forces and TBO is easily released, leading to a total annihilation (100 %) of *E. coli* colonies compared to the control (**** significance level in every case). However, the results obtained for TBO-Glu@CNC-w, which underwent extensive washing with 1 M NaCl to remove electrostatically absorbed TBO molecules, diverged significantly. In this case, the dark toxicity was minimized (83 % CFU), indicating that CNC can mitigate the inherent toxicity of free TBO in dark conditions while maintaining a moderate phototoxic effect (41 % CFU) under red light irradiation (*** significance level). Thus, the CNC nanoplatform could be considered a potential carrier to overcome some of the limitations of PSs in aPDT, such as poor solubility, targeting, and high dark toxicity.

4. Conclusion

In this study, we investigated the potential of photosensitized cellulose nanocrystals (CNC) as a novel platform for antimicrobial photodynamic therapy (aPDT) against Gram-negative bacteria, particularly *Escherichia coli* (*E. coli*). The covalent functionalization of CNC with anionic (Rose Bengal: RB) or cationic (Toluidine Blue O: TBO) photosensitizers, along with *N*-alkyl-D-gluconamide, a scarcely investigated open-chain carbohydrate ligand for selective targeting of Gram-negative bacteria, was achieved using efficient trialkoxysilane linker chemistry. The synthesized nanomaterials exhibited high PS loading, good stability in aqueous media, and stable covalent linkage of the PSs to CNC. The photophysical properties of both PSs remained largely unaltered when anchored to CNC, including the effective generation of reactive oxygen species (ROS) for antimicrobial photodynamic therapy. The photosensitized RB-Glu@CNC and RB@CNC nanoplatforms exhibited superior phototoxicity against *E. coli* under green light irradiation, while mitigating the dark toxicity associated with the PS. The presence of gluconamide further enhanced the phototoxicity of RB-Glu@CNC, underscoring the importance of surface functionalization for improved efficacy. In comparison, TBO-Glu@CNC showed moderate antimicrobial activity under red light irradiation after extensive washing to remove
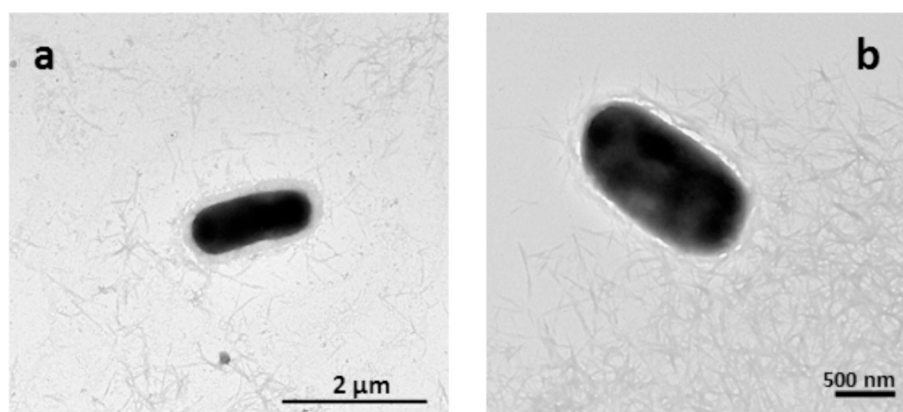
Fig. 7. Representative TEM image of a fixed *E. coli* bacteria exposed to nanocellulose at 0.15 mg/mL of CNC (a) and Glu@CNC (b). Scale bar 2 μm and 500 nm.
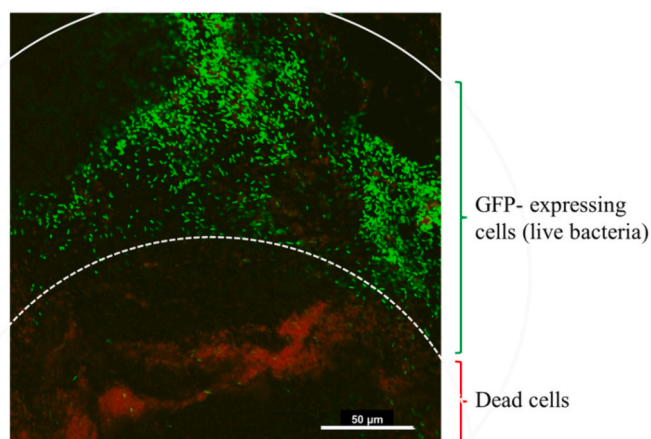

Fig. 8. Confocal microscopy image illustrating GFP-expressing *E. coli* incubated in an agar plate and exposed to RB-Glu@CNC. The culture plate partially exposed to light. A solid white line delineates the edge of the culture plate and dashed lines mark the light-irradiated region. The upper segment, shielded from light to maintain darkness, shows bright green GFP-expressing bacteria, whereas the irradiated area shows no fluorescence, indicating no active or dead cells.

electrostatically absorbed PS. CNC attachment also significantly mitigated the inherent dark toxicity observed for free TBO. Furthermore, the RB@CNC and RB-Glu@CNC systems displayed significant fluorescence emission suitable for tracking via fluorescence microscopy, making them promising nanomaterials for theranostics, integrating bioimaging and aPDT. Overall, photosensitized CNC shows significant potential as a carrier for addressing topical infections caused by Gram-negative bacteria, while also minimizing the side effects linked to conventional PSs. Further enhancements in PS loading and surface functionalization methods, coupled with investigations into cytocompatibility and mechanism of action, offer promise for developing effective and safe therapeutic alternatives against multidrug-resistant pathogens.

CRediT authorship contribution statement

Ruth Prieto-Montero: Writing – original draft, Methodology, Investigation. **Maite Tejón:** Methodology, Investigation. **Andrea Albaya:** Methodology, Investigation. **Teresa Arbeloa:** Investigation. **Jose Luis Chiara:** Writing – review & editing, Project administration, Investigation, Funding acquisition. **Mónica L. Fanarraga:** Writing – review & editing, Supervision, Methodology, Investigation, Funding acquisition. **Virginia Martínez-Martínez:** Writing – review & editing, Supervision, Project administration, Investigation, Funding acquisition,
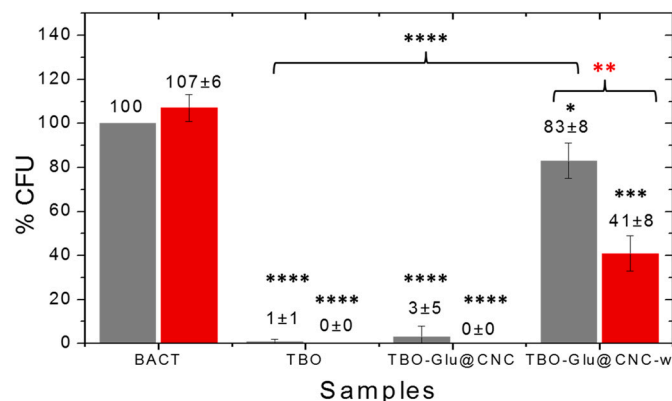
Fig. 9. CFU % (as test of viability) of *E. coli* bacteria in dark (grey bar) and under 2 h of red irradiation (red bar) incubated with different systems: nothing (BACT), TBO-free in solution at the concentration of $5 \cdot 10^{-7}$ M (TBO), TBO-Glu@CNC with TBO covalent and electrostatic attached, and TBO-Glu@CNC-w with TBO only covalently attached, respectively. The TBO concentration was in every system $5 \cdot 10^{-7}$ M and 2 h of incubation (and light exposition for the irradiated samples). Black asterisks indicate a significant difference compared to controls. Red asterisks indicate significant differences between dark and light conditions at the same concentrations tested. *P* value: *<0.033, **<0.002, ***<0.0002, and ****<0.0001, $n = 3$, DF = 4.

Data curation, Conceptualization.

Declaration of competing interest

The authors declare that they have no known competing financial interests or personal relationships that could have appeared to influence the work reported in this paper.

Data availability

Data will be made available on request.

Acknowledgments

Next generation), and FPI fellowship (PRE2021-098894), respectively.

Appendix A. Supplementary data

References

Abderrahim, B., Abderrahman, E., Mohamed, A., Fatima, T., Abdesselam, T., & Krim, O. (2015). Kinetic thermal degradation of cellulose, polybutylene succinate and a green composite: Comparative study. *World Journal of Environmental Engineering, 3*(4), 95–110. https://doi.org/10.12691/WJEE-3-4-1. Vol. 3, 2015, Pages 95–110.

Al-Majmaie, R., Alattar, N., Zerulla, D., & Al-Rubeai, M. (2012). Toluidine blue O-conjugated gold nanoparticles for photodynamic therapy of cultured colon cancer. In J. Popp, W. Drexler, V. V. Tuchin, & D. L. Matthews (Eds.), *Vol. 84271. Biophotonics: Photonic solutions for better health care III* (p. 842722). https://doi.org/10.1117/12.921813. Al-.

Alvarado, D. R., Argyropoulos, D. S., Scholle, F., Peddinti, B. S. T., & Ghiladi, R. A. (2019). A facile strategy for photoactive nanocellulose-based antimicrobial materials. *Green Chemistry, 21*(12), 3424–3435. https://doi.org/10.1039/c9gc00551j

Antoñanzas, F., & Goossens, H. (2019). The economics of antibiotic resistance: A claim for personalised treatments. *The European Journal of Health Economics, 20*(4), 483–485. https://doi.org/10.1007/s10198-018-1021-z

Arulprakasajothi, M., Elangovan, K., Chandrasekhar, U., & Suresh, S. (2018). Performance study of conical strip inserts in tube heat. *Thermal Science, 22*(1), 477–485. https://doi.org/10.2298/TSCI151024250A

Atrash, M., Hovor, I., Gurianov, Y., Barel, M., Semenova, O., Brider, T., … Nakonechny, F. (2024). Antibacterial properties of Rose Bengal conjugated to hyaluronic acid. *International Journal of Molecular Sciences, 25*(6). https://doi.org/10.3390/ijms25063330

Awad, M., Thomas, N., Barnes, T. J., & Prestidge, C. A. (2022). Nanomaterials enabling clinical translation of antimicrobial photodynamic therapy. *Journal of Controlled Release, 346*, 300–316. https://doi.org/10.1016/j.jconrel.2022.04.035

Banin, E., Hughes, D., & Kuipers, O. P. (2017). Editorial: Bacterial pathogens, antibiotics and antibiotic resistance. *FEMS Microbiology Reviews, 41*(3), 450–452. https://doi.org/10.1093/femsre/fux016

Bhattacharjee, S. (2016). DLS and zeta potential - what they are and what they are not? *Journal of Controlled Release, 235*, 337–351. https://doi.org/10.1016/j.jconrel.2016.06.017

Blázquez-Moraleja, A., Moya, P., Marin, M. L., & Bosca, F. (2023). Synthesis of novel heterogeneous photocatalysts based on Rose Bengal for effective wastewater disinfection and decontamination. *Catalysis Today, 413–415*, Article 113948. https://doi.org/10.1016/j.cattod.2022.11.009

Brinkmann, A., Chen, M., Couillard, M., Jakubek, Z. J., Leng, T., & Johnston, L. J. (2016). Correlating cellulose nanocrystal particle size and surface area. *Langmuir, 32*(24), 6105–6114. https://doi.org/10.1021/acs.langmuir.6b01376

Broekgaarden, M., Weijer, R., van Gulik, T. M., Hamblin, M. R., & Heger, M. (2015). Tumor cell survival pathways activated by photodynamic therapy: A molecular basis for pharmacological inhibition strategies. *Cancer and Metastasis Reviews, 34*(4), 643–690. https://doi.org/10.1007/s10555-015-9588-7

Capeletti, L. B., de Oliveira, J. F. A., Loiola, L. M. D., Galdino, F. E., da Silva Santos, D. E., Soares, T. A., … Cardoso, M. B. (2019). Gram-negative bacteria targeting mediated by carbohydrate–carbohydrate interactions induced by surface-modified nanoparticles. *Advanced Functional Materials, 29*(48), 1–11. https://doi.org/10.1002/adfm.201904216

Carrera, E. T., Dias, H. B., Corbi, S. C. T., Marcantonio, R. A. C., Bernardi, A. C. A., Bagnato, V. S., … Rastelli, A. N. S. (2016). The application of antimicrobial photodynamic therapy (aPDT) in dentistry: A critical review. *Laser Physics, 26*(12), Article 123001. https://doi.org/10.1088/1054-660X/26/12/123001

Cassini, A., Högberg, L. D., Plachouras, D., Quattrocchi, A., Hoxha, A., Simonsen, G. S., … Hopkins, S. (2019). Attributable deaths and disability-adjusted life-years caused by infections with antibiotic-resistant bacteria in the EU and the European Economic Area in 2015: A population-level modelling analysis. *The Lancet Infectious Diseases, 19*(1), 56–66. https://doi.org/10.1016/S1473-3099(18)30605-4

Chauhan, P., & Yan, N. (2015). Nanocrystalline cellulose grafted phthalocyanine: A heterogeneous catalyst for selective aerobic oxidation of alcohols and alkyl arenes at room temperature in a green solvent. *RSC Advances, 5*(47), 37517–37520. https://doi.org/10.1039/c4ra16869k

Chen, J., Cesario, T. C., & Rentzepis, P. M. (2010). Time resolved spectroscopic studies of methylene blue and phenothiazine derivatives used for bacteria inactivation. *Chemical Physics Letters, 498*(1–3), 81–85. https://doi.org/10.1016/j.cplett.2010.08.042

Chen, Y., Zhang, Z., Sui, X., Brennan, J. D., & Brook, M. A. (2005). Reduced shrinkage of sol-gel derived silicas using sugar-based silsesquioxane precursors. *Journal of Materials Chemistry, 15*(30), 3132–3141. https://doi.org/10.1039/b502959g

Dahl, T. A., Midden, W. R., & Hartman, P. E. (1989). Comparison of killing of gram-negative and gram-positive bacteria by pure singlet oxygen. *Journal of Bacteriology, 171*(4), 2188–2194. https://doi.org/10.1128/jb.171.4.2188-2194.1989

Dahl, T. A., Midden, W. R., & Neckers, D. C. (1988). Comparison of photodynamic action by Rose Bengal in Gram-positive and Gram-negative bacteria. *Photochemistry and Photobiology, 48*(5), 607–612. https://doi.org/10.1111/j.1751-1097.1988.tb02870.x

Dai, X., Du, T., & Han, K. (2019). Engineering nanoparticles for optimized photodynamic therapy. *ACS Biomaterials Science and Engineering, 5*(12), 6342–6354. https://doi.org/10.1021/acsbiomaterials.9b01251

Das, S., Ghosh, B., & Sarkar, K. (2022). Nanocellulose as sustainable biomaterials for drug delivery. *Sensors International, 3*, Article 100135. https://doi.org/10.1016/j.sintl.2021.100135

Decraene, V., Pratten, J., & Wilson, M. (2006). Cellulose acetate containing toluidine blue and Rose Bengal is an effective antimicrobial coating when exposed to white light. *Applied and Environmental Microbiology, 72*(6), 4436–4439. https://doi.org/10.1128/AEM.02945-05

Demidova, T. N., & Hamblin, M. R. (2005). Effect of cell-photosensitizer binding and cell density on microbial photoinactivation. *Antimicrobial Agents and Chemotherapy, 49*(6), 2329–2335. https://doi.org/10.1128/AAC.49.6.2329-2335.2005

DeRosa, M. (2002). Photosensitized singlet oxygen and its applications. *Coordination Chemistry Reviews, 233–234*, 351–371. https://doi.org/10.1016/S0010-8545(02)00034-6

Do, T. T. A., Grijalvo, S., Imae, T., Garcia-Celma, M. J., & Rodríguez-Abreu, C. (2021). A nanocellulose-based platform towards targeted chemo-photodynamic/photothermal cancer therapy. *Carbohydrate Polymers, 270*, Article 118366. https://doi.org/10.1016/j.carbpol.2021.118366

Feese, E., Sadeghifar, H., Gracz, H. S., Argyropoulos, D. S., & Ghiladi, R. A. (2011). Photobactericidal porphyrin-cellulose nanocrystals: Synthesis, characterization, and antimicrobial properties. *Biomacromolecules, 12*, 3528–3539.

García-Hevia, L., Saramiforoshani, M., Monge, J., Iturrioz-Rodríguez, N., Padín-González, E., González, F., … Fanarraga, M. L. (2021). The unpredictable carbon nanotube biocorona and a functionalization method to prevent protein biofouling. *Journal of Nanobiotechnology, 19*(1), 1–13. https://doi.org/10.1186/s12951-021-00872-x

George, S., Hamblin, M. R., & Kishen, A. (2009). Uptake pathways of anionic and cationic photosensitizers into bacteria. *Photochemical & Photobiological Sciences, 8*(6), 788–795. https://doi.org/10.1039/b809624d

Hemraz, U. D., Campbell, K. A., Burdick, J. S., Ckless, K., Boluk, Y., & Sunasee, R. (2015). Cationic poly(2-aminoethylmethacrylate) and poly(N-(2-aminoethylmethacrylamide)) modified cellulose nanocrystals: Synthesis, characterization, and cytotoxicity. *Biomacromolecules, 16*, 319–325.

Hu, X., Huang, Y. Y., Wang, Y., Wang, X., & Hamblin, M. R. (2018). Antimicrobial photodynamic therapy to control clinically relevant biofilm infections. *Frontiers in Microbiology, 9*(JUN), 1–24. https://doi.org/10.3389/fmicb.2018.01299

Ji, Y., Yang, X., Ji, Z., Zhu, L., Ma, N., Chen, D., … Cao, Y. (2020). DFT-calculated IR spectrum amide I, II, and III band contributions of N-methylacetamide fine components. *ACS Omega, 5*(15), 8572–8578. https://doi.org/10.1021/acsomega.9b04421

Jørgensen, P. S., Wernli, D., Carroll, S. P., Dunn, R. R., Harbarth, S., Levin, S. A., … Laxminarayan, R. (2016). Use antimicrobials wisely. *Nature, 537*(7619), 159–161. https://doi.org/10.1038/537159a

Kaya, G. G., Medaglia, S., Candela-Noguera, V., Tormo-Mas, M.Á., Marcos, M. D., Aznar, E., … Martínez-Máñez, R. (2020). Antibacterial activity of linezolid against gram-negative bacteria: Utilization of ε-poly-l-lysine capped silica xerogel as an activating carrier. *Pharmaceutics, 12*(11), 1–14. https://doi.org/10.3390/pharmaceutics12111126

Klausen, M., Ucuncu, M., & Bradley, M. (2020). Design of photosensitizing agents for targeted antimicrobial photodynamic therapy. *Molecules, 25*(22), 5239. https://doi.org/10.3390/molecules25225239

Klemm, D., Heublein, B., Fink, H.-P., & Bohn, A. (2005). Cellulose: Fascinating biopolymer and sustainable raw material. *Angewandte Chemie International Edition, 44*(22), 3358–3393. https://doi.org/10.1002/anie.200460587

Kömerik, N., Wilson, M., & Poole, S. (2000). The effect of photodynamic action on two virulence factors of gram-negative bacteria. *Photochemistry and Photobiology, 72*(5), 676. https://doi.org/10.1562/0031-8655(2000)072<0676:TEOPAO>2.0.CO;2

Koshani, R., Zhang, J., Van De Ven, T. G. M., Lu, X., & Wang, Y. (2021). Modified hairy nanocrystalline cellulose as photobactericidal nanofillers for food packaging application. *ACS Sustainable Chemistry and Engineering, 9*(31), 10513–10523. https://doi.org/10.1021/acssuschemeng.1c02289

Kurosu, M., Mitachi, K., Yang, J., Pershing, E. V., Horowitz, B. D., Wachter, E. A., … Rodrigues, D. J. (2022). Antibacterial activity of pharmaceutical-grade Rose Bengal: An application of a synthetic dye in antibacterial therapies. *Molecules, 27*(1). https://doi.org/10.3390/molecules27010322

Lacey, J. A., & Phillips, D. (2001). The photosensitisation of Escherichia coli using disulphonated aluminium phthalocyanine. *Journal of Photochemistry and Photobiology A: Chemistry, 142*(2–3), 145–150. https://doi.org/10.1016/S1010-6030(01)00508-1

Lacombe, S., & Pigot, T. (2016). Materials for selective photo-oxygenation vs. photocatalysis: Preparation, properties and applications in environmental and health fields. *Catalysis Science & Technology, 6*(6), 1571–1592. https://doi.org/10.1039/C5CY01929J

Laxminarayan, R., Matsoso, P., Pant, S., Brower, C., Røttingen, J. A., Klugman, K., & Davies, S. (2016). Access to effective antimicrobials: A worldwide challenge. *The Lancet, 387*(10014), 168–175. https://doi.org/10.1016/S0140-6736(15)00474-2

Lucky, S. S., Soo, K. C., & Zhang, Y. (2015). Nanoparticles in photodynamic therapy. *Chemical Reviews, 115*(4), 1990–2042. https://doi.org/10.1021/cr5004198

Luepke, K. H., Suda, K. J., Boucher, H., Russo, R. L., Bonney, M. W., Hunt, T. D., & Mohr, J. F. (2017). Past, present, and future of antibacterial economics: Increasing bacterial resistance, limited antibiotic pipeline, and societal implications. *Pharmacotherapy: The Journal of Human Pharmacology and Drug Therapy, 37*(1), 71–84. https://doi.org/10.1002/phar.1868

Magde, D., Brannon, J. H., Cremers, T. L., & Olmsted, J. (1979). Absolute luminescence yield of cresyl violet. A standard for the red. *Journal of Physical Chemistry, 83*(6), 696–699. https://doi.org/10.1021/j100469a012

Malekpour, K., Hazrati, A., Khosrojerdi, A., Roshangar, L., & Ahmadi, M. (2023). An overview to nanocellulose clinical application: Biocompatibility and opportunities in disease treatment. *Regenerative Therapy, 24*, 630–641. https://doi.org/10.1016/j.reth.2023.10.006

Manoil, D., Filieri, A., Schrenzel, J., & Bouillaguet, S. (2016). Rose bengal uptake by E. faecalis and F. nucleatum and light-mediated antibacterial activity measured by flow cytometry. *Journal of Photochemistry and Photobiology B: Biology, 162*, 258–265. https://doi.org/10.1016/j.jphotobiol.2016.06.042

Mariño-Ocampo, N., Reyes, J. S., Günther, G., Heyne, B., & Fuentealba, D. (2022). Thiol-reacting toluidine blue derivatives: Synthesis, photophysical properties and covalent conjugation with human serum albumin. *Dyes and Pigments, 201*, 1–9. https://doi.org/10.1016/j.dyepig.2022.110225

Martínez, C. G., Braun, A. M., & Oliveros, E. (2004). Effect of the media on the quantum yield of singlet oxygen (O 2(1Δg)) production by 9H-fluoren-9-one: Microheterogeneous systems. *Helvetica Chimica Acta, 87*(2), 382–393. https://doi.org/10.1002/hlca.200490036

Mas, N., Galiana, I., Mondragón, L., Aznar, E., Climent, E., Cabedo, N., … Amorós, P. (2013). Enhanced efficacy and broadening of antibacterial action of drugs via the use of capped mesoporous nanoparticles. *Chemistry - A European Journal, 19*(34), 11167–11171. https://doi.org/10.1002/chem.201302170

Mirzahosseinipour, M., Khorsandi, K., Hosseinzadeh, R., Ghazaeian, M., & Shahidi, F. K. (2020). Antimicrobial photodynamic and wound healing activity of curcumin encapsulated in silica nanoparticles. *Photodiagnosis and Photodynamic Therapy, 29*, Article 101639. https://doi.org/10.1016/j.pdpdt.2019.101639

Monteiro, C. J. P., Neves, M. G. P. M. S., Nativi, C., Almeida, A., & Faustino, M. A. F. (2023). Porphyrin photosensitizers grafted in cellulose supports: A review. *International Journal of Molecular Sciences, 24*(4), 3475. https://doi.org/10.3390/ijms24043475

Navarro, J. R. G., & Bergström, L. (2014). Labelling of N-hydroxysuccinimide-modified rhodamine B on cellulose nanofibrils by the amidation reaction. *RSC Advances, 4*(105), 60757–60761. https://doi.org/10.1039/C4RA06559J

Nikaido, H. (2009). Multidrug resistance in bacteria. *Annual Review of Biochemistry, 78*(1), 119–146. https://doi.org/10.1146/annurev.biochem.78.082907.145923

Nonell, S., & Flors, C. (2016). In S. Nonell, & C. Flors (Eds.), *Vol. 2. Singlet oxygen, applications in biosciences and Nanosciences*. Cambridge: Royal Society of Chemistry. http://ebook.rsc.org/?DOI=10.1039/9781782622208.

Pinto, R. J. B., Lameirinhas, N. S., Guedes, G., da Silva, G. H. R., Oskoei, P., Spirk, S., … Freire, C. S. R. (2021). Cellulose nanocrystals/chitosan-based nanosystems: Synthesis, characterization, and cellular uptake on breast cancer cells. *Nanomaterials, 11*(8). https://doi.org/10.3390/nano11082057

Planas, O., Bresolí-Obach, R., Nos, J., Gallavardin, T., Ruiz-González, R., Agut, M., & Nonell, S. (2015). Synthesis, photophysical characterization, and photoinduced antibacterial activity of methylene blue-loaded amino- and mannose-targeted mesoporous silica nanoparticles. *Molecules, 20*(4), 6284–6298. https://doi.org/10.3390/molecules20046284

Prieto, J. B., Arbeloa, F. L., Martínez, V. M., López, T. A., & Arbeloa, I. L. (2004). Photophysical properties of the pyrromethene 597 dye: Solvent effect. *Journal of Physical Chemistry A, 108*(26), 5503–5508. https://doi.org/10.1021/jp0373898

Prieto-Montero, R., Arbeloa, T., & Martínez-Martínez, V. (2023). Photosensitizer-mesoporous silica nanoparticles combination for enhanced photodynamic therapy (PDT). *Photochemistry and Photobiology, 99*(3), 882–900. https://doi.org/10.1111/php.13802

Prieto-Montero, R., Prieto-Castañeda, A., Katsumiti, A., Cajaraville, M. P., Agarrabeitia, A. R., Ortiz, M. J., & Martínez-Martínez, V. (2021). Functionalization of photosensitized silica nanoparticles for advanced photodynamic therapy of cancer. *International Journal of Molecular Sciences, 22*(12), 6618–6641. https://doi.org/10.3390/ijms22126618

Prieto-Montero, R., Prieto-Castañeda, A., Katsumiti, A., Sola-Llano, R., Agarrabeitia, A. R., Cajaraville, M. P., … Martinez-Martinez, V. (2022). Red haloBODIPYs as theragnostic agents: The role of the substitution at meso position. *Dyes and Pigments, 198*, Article 110015. https://doi.org/10.1016/j.dyepig.2021.110015

Pucelik, B., & Dąbrowski, J. M. (2022). Photodynamic inactivation (PDI) as a promising alternative to current pharmaceuticals for the treatment of resistant microorganisms. *Advances in Inorganic Chemistry, 79*, 65–108. https://doi.org/10.1016/bs.adioch.2021.12.003

Q. Mesquita, M., J. Dias, C., P. M. S. Neves, M., Almeida, A., & F. Faustino, M. (2018). Revisiting current photoactive materials for antimicrobial photodynamic therapy. *Molecules, 23*(10), 2424. https://doi.org/10.3390/molecules23102424

Qiao, Y., Geng, H., Jiang, N., Zhu, X., Li, C., & Cai, Q. (2020). Polymyxin B–modified upconversion nanoparticles for selective detection of Gram-negative bacteria such as Escherichia coli. *Journal of Chemical Research, 44*(11–12), 756–761. https://doi.org/10.1177/1747519820911266

Ran, B., Wang, Z., Cai, W., Ran, L., Xia, W., Liu, W., & Peng, X. (2021). Organic photo-antimicrobials: Principles, molecule design, and applications. *Journal of the American Chemical Society, 143*(43), 17891–17909. https://doi.org/10.1021/jacs.1c08679

Rizzi, V., Losito, I., Ventrella, A., Fini, P., Fraix, A., Sortino, S., … Cosma, P. (2015). Rose Bengal-photosensitized oxidation of 4-thiothymidine in aqueous medium: Evidence for the reaction of the nucleoside with singlet state oxygen. *Physical Chemistry Chemical Physics, 17*(39), 26307–26319. https://doi.org/10.1039/C5CP03615A

Sabbahi, S., Ben Ayed, L., & Jemli, M. (2018). Staphylococcus aureus photodynamic inactivation mechanisms by rose bengal: Use of antioxidants and spectroscopic study. *Applied Water Science, 8*(2), 1–9. https://doi.org/10.1007/s13201-018-0693-y

Sarbadhikary, P., George, B. P., & Abrahamse, H. (2021). Recent advances in photosensitizers as multifunctional theranostic agents for imaging-guided photodynamic therapy of cancer. *Theranostics, 11*(18), 9054–9088. https://doi.org/10.7150/thno.62479

Sommer, A., & Staroszczyk, H. (2023). Bacterial cellulose vs. bacterial cellulose nanocrystals as stabilizer agents for O/W Pickering emulsions. *Food Hydrocolloids, 145*(March), Article 109080. https://doi.org/10.1016/j.foodhyd.2023.109080

Songca, S. P., & Adjei, Y. (2022). Applications of antimicrobial photodynamic therapy against bacterial biofilms. *International Journal of Molecular Sciences, 23*(6), 3209. https://doi.org/10.3390/ijms23063209

Sułek, A., Pucelik, B., Kobielusz, M., Łabuz, P., Dubin, G., & Dąbrowski, J. M. (2019). Surface modification of nanocrystalline TiO$_2$ materials with sulfonated porphyrins for visible light antimicrobial therapy. *Catalysts, 9*(10), 821. https://doi.org/10.3390/catal9100821

Tacconelli, E., Carrara, E., Savoldi, A., Harbarth, S., Mendelson, M., Monnet, D. L., … Zorzet, A. (2018). Discovery, research, and development of new antibiotics: The WHO priority list of antibiotic-resistant bacteria and tuberculosis. *The Lancet Infectious Diseases, 18*(3), 318–327. https://doi.org/10.1016/S1473-3099(17)30753-3

Thanh, N. T. K., & Green, L. A. W. (2010). Functionalisation of nanoparticles for biomedical applications. *Nano Today, 5*(3), 213–230. https://doi.org/10.1016/j.nantod.2010.05.003

Triesscheijn, M., Baas, P., Schellens, J. H. M., & Stewart, F. A. (2006). Photodynamic therapy in oncology. *The Oncologist, 11*(9), 1034–1044. https://doi.org/10.1634/theoncologist.11-9-1034

Vilarinho, F., Sanches Silva, A., Vaz, M. F., & Farinha, J. P. (2017). Nanocellulose in green food packaging. *Critical Reviews in Food Science and Nutrition, 8398*(July), 1–12. https://doi.org/10.1080/10408398.2016.1270254

Willyard, C. (2017). Drug-resistant bacteria ranked. *Nature, 543*, 15.

Wright, G. D. (2015). Solving the antibiotic crisis. *ACS Infectious Diseases, 1*(2), 80–84. https://doi.org/10.1021/id500052s

Wu, H., Wang, W., Zhang, Z., Li, J., Zhao, J., Liu, Y., … Wang, S. (2020). Synthesis of a clay-based nanoagent for photonanomedicine. *ACS Applied Materials and Interfaces, 12*(1), 390–399. https://doi.org/10.1021/acsami.9b19930

Yin, R., & Hamblin, M. (2015). Antimicrobial photosensitizers: Drug discovery under the spotlight. *Current Medicinal Chemistry, 22*(18), 2159–2185. https://doi.org/10.2174/0929867322666150319120134

Zhao, Z., Yan, R., Wang, J., Wu, H., Wang, Y., Chen, A., … Li, Y. Q. (2017). A bacteria-activated photodynamic nanosystem based on polyelectrolyte-coated silica nanoparticles. *Journal of Materials Chemistry B, 5*(19), 3572–3579. https://doi.org/10.1039/c7tb00199a